PHYSICAL REVIEW B **89**, 035306 (2014)

Electronic properties of δ-doped Si:P and Ge:P layers in the high-density limit using a Thomas-Fermi method

J. S. Smith,* J. H. Cole,† and S. P. Russo‡

Chemical and Quantum Physics, School of Applied Sciences, RMIT University, Melbourne VIC 3001, Australia

(Received 28 August 2013; revised manuscript received 17 December 2013; published 13 January 2014)

We present a scalable method for calculating the electronic properties of a δ-doped phosphorus layer in silicon and germanium. Our calculations are based on an $sp^3d^5s^*$ tight-binding model and the Thomas-Fermi-Dirac approximation. The energy shift in the lowest conduction band states of the Ge band structure is characterized and a comparison is made to a δ-doped P layer in Si. The results for the δ-doped Si:P layer themselves compare well to the predictions of more "resource intensive" computational models. The Thomas-Fermi method presented herein scales easily to large system sizes. Efficient scaling is important for the calculation of quantum transport properties in δ-doped semiconductors that are currently of experimental interest.

DOI: 10.1103/PhysRevB.89.035306 PACS number(s): 71.10.Ca, 31.15.aq, 73.22.−f, 71.15.−m

I. INTRODUCTION

New *in situ* phosphorus δ-doping techniques in single crystalline silicon and germanium are achieving unprecedented carrier concentrations inside highly confined layers (δ layers) of the host material [1,2]. δ-doped P layers in Si (Si:P) and Ge (Ge:P) are ideally one monolayer (ML) thick and, at very low temperatures, exhibit electronic properties that are a combination of those of the dopant and the host material. Through advances in scanning tunneling microscope lithography [3] and molecular beam epitaxy [4], a new generation of δ-doped structures is now being realized. These structures include; δ-doped Si:P layers [5], quantum dots [6,7], quantum wires [8–10], and δ-doped Ge:P layers [11,12].

Using *in situ* doping techniques one in four (1/4) atoms inside a Si(001) ML can be replaced with a substitutional P donor [1]. The arrangement of the P atoms inside the dopant plane is inherently disordered [1] and, therefore, at these high doping densities, we expect the donor electrons to behave similarly to an inhomogeneous electron gas. However, the majority of recent computational models of Si:P δ layers describe the donor electrons *via* explicit ordered/disordered arrangements of the P atoms rather than an average donor electron density. Experimental verification of either type of model is currently unavailable as recent measurements of the Si:P δ layer band structure are inconclusive when compared to the theory [13]. Presently, therefore, it is only through computational modeling that we can quantitatively investigate the electronic properties of these Si:P and Ge:P δ layers.

Ge:P δ layers have recently been made with two-dimensional (2D) carrier concentrations of 1/2–1/4 ML [11,12]. These extremely high doping densities are characteristic of complete substitutional P-doping of the Ge(001) surface [2]. Currently, however, there is no empirical model for the electronic properties of these novel Ge:P nanostructures. Here, we fill in the gap in the literature by applying a Thomas-Fermi (TF) method to a Ge:P δ layer and compare the results to those of a Si:P δ layer. There is an *a priori* argument for applying our TF method to a Ge:P δ layer as unlike density functional theory (DFT) [14], tight-binding (TB) methods are able to reproduce the band structure of bulk Ge as easily as that of bulk Si (without the need for *ad hoc* adjustment of the on-site atomic energies as in, for example, LDA+U [15]).

Recent empirical and *ab initio* models of Si:P δ layers are designed to maximize the completeness of the system's mathematical description rather than minimize the use of computational resources. Here, we show the results of these methods to be reproducible by a less "resource intensive" TF model of the donor potential combined with a TB description of the host material [16]. This TF method scales easily to the large system sizes that are needed for the calculation of quantum transport properties in δ-doped semiconductors.

Although a semiclassical model of electronic transport in Si:P δ layers was reported recently [17], computational models of quantum transport in Si:P and Ge:P δ layers are strangely absent from the literature. Such theoretical models would provide a means of comparison between theory and experiment, something which is sorely lacking in the present generation of Si:P δ layer models. The nonequilibrium Green's functions formalism could be used to model transport in these systems [18]. However, this formalism requires the nanostructures to be divided into source, drain and channel regions, and results in large system sizes. It is therefore necessary to combine this formalism with a theoretical model of δ-doped semiconductors that is computationally inexpensive, such as those based on TF or effective mass theory (EMT). Unfortunately, although inexpensive, the EMT can only be applied to the lowest conduction band (CB) states (which exhibit parabolic dispersion) and is therefore not able to describe the higher CB states or their effect on transport in these systems.

In this paper, we present a scalable method for calculating the electronic properties of Si:P and Ge:P δ layers. Our TF method is based on the Thomas-Fermi-Dirac (TFD) approximation and an $sp^3d^5s^*$ TB model. We first calculate the electronic properties of a Si:P δ layer to: (a) benchmark the TF method for these δ-doped systems, and (b) provide a means of comparison for the Ge:P δ layer. We then calculate the electronic properties of a Ge:P δ layer, reporting on the band structure, Fermi level, valley splitting, binding energy, electronic density of states (eDOS) and the variation in these

*jackson.smith@rmit.edu.au

†jared.cole@rmit.edu.au

‡salvy.russo@rmit.edu.au

 ©2014 American Physical Society

properties with doping density. The TF method is outlined in Sec. II. The results of the method's application to a Si:P δ layer are discussed in Sec. III and to a Ge:P δ layer in Sec. IV. We conclude in Sec. V.

II. METHODOLOGY

A. Hamiltonian of the bulk system

The electronic properties of the bulk Si and Ge are described in the TB approximation. The Hamiltonian is defined using an $sp^3d^5s^*$ basis set with 18 empirical parameters [19] that correctly predict the bulk effective masses of Si and Ge [16]. The Hamiltonian is of the form

$$\hat{H}_{\text{bulk}} = \sum_{i,u} \varepsilon_i^{(u)} c_{i,u}^\dagger c_{i,u} + \sum_{i,j\neq i,u,v} t_{ij}^{(uv)} c_{i,u}^\dagger c_{j,v} + \hat{H}_{\text{b.c.}}, \quad (1)$$

where $c_{i,u}^\dagger$ and $c_{i,u}$ are creation and annihilation operators, respectively. The first term in Eq. (1) describes the on-site energies ($\varepsilon_i^{(u)}$) of an electron in orbital u on atom i and the second term the coupling ($t_{ij}^{(uv)}$) between electron orbitals u and v on first nearest-neighbor atoms i and j. The third term ($\hat{H}_{\text{b.c.}}$) describes the boundary conditions, which for periodic boundaries are of the form

$$\hat{H}_{\text{b.c.}} = \sum_{k,l\neq k,u,v} t_{kl}^{(uv)} c_{k,u}^\dagger c_{l,v}, \quad (2)$$

where k and l are first nearest-neighbor atoms *via* the periodic boundaries of the supercell. The Hamiltonian terms $\varepsilon_i^{(u)}$ and $t_{ij}^{(uv)}$ are defined in terms of TB parameters [20]. These parameters are determined through an optimization procedure that fits to experimentally measured band energies and effective masses at high-symmetry points in the Brillouin zone (BZ) [21]. We do not carry out such a procedure here but instead use previously published TB parameters for Si and Ge [16].

The $sp^3d^5s^*$ basis set comprizes 20 hydrogenic orbitals for the description of the bulk Si and Ge band structure. In the Si:P δ layer, the P donor electrons occupy CB states that are nondegenerate [13] and, therefore, we are able to ignore electron spin and halve the size of the TB basis set from 20 to 10 orbitals. This results in a Hamiltonian matrix of order 4800×4800. To calculate the electronic properties of the δ layers, the Hamiltonian matrix is diagonalized for all $\vec{k}$ points in the first irreducible Brillouin zone (IBZ) [22]. The speed of this diagonalization is directly proportional to the order of the Hamiltonian matrix and the number of $\vec{k}$ points sampled in the first 2D BZ or $\vec{k}$-point grid. We use a $\vec{k}$-point grid of $120 \times 120 \times 1$ to converge the Fermi level to within 1 meV.

To simulate the δ layer, we use a primitive tetragonal (PT) supercell, which has dimensions $a \times a \times 60a$, where a is the lattice constant of the host material. This is equivalent to 120 MLs of bulk "cladding" in the positive and negative z directions perpendicular to the dopant plane. Periodic boundary conditions are applied in the x and y directions, and also in the z direction after the bulk cladding. Using 120 MLs of bulk cladding in the z direction, the energies of the CB states of interest are converged to within 1 meV. We do not geometry optimize the bulk Si or Ge surrounding the δ layer as previous DFT investigations have shown that the effect of the P atoms on the positions of the bulk Si atoms is negligible [23,24]. However, we expect the incorporation of P atoms into bulk Ge to have a larger effect on the positions of the Ge atoms because the Ge nucleus is much larger than the Si and P nuclei. Also, although we do not geometry optimize the bulk Ge here, we acknowledge that this approximation requires further investigation.

TABLE I. Parameters used in the calculations. m_0 is the free electron mass.

	ϵ_r	m_l/m_0	m_t/m_0	a (Å)
Si	11.4[a]	0.9163[b]	0.1905[b]	5.430[c]
Ge	15.36[a]	1.588[d]	0.08152[d]	5.6563[c]

[a]Reference [25].
[b]Reference [26].
[c]Reference [16].
[d]Reference [27].

B. Hamiltonian of the doped system

The donor electrons are described by a 1D potential that is added to the on-site energies or diagonal terms of the Hamiltonian matrix [28,29]. The TFD approximation and a parametrization of correlation effects are used to calculate the potential energy of the donor electrons. The dopant plane is approximated by an infinitely thin sheet with a constant areal doping density. The validity of the local density approximation (LDA) is assumed throughout. Within the LDA, the TFD approximation is exact in the high-density limit. The TF theory of δ-doped semiconductors has been shown to produce meaningful results for doping densities in the range of 10^{12}–10^{13}cm^{-2} (one to two orders of magnitude lower than the doping densities considered here) [30]. A derivation of the TF theory for δ-doped semiconductors is given in Appendix. The parameters in Table I are used throughout.

For a 2D δ-doped semiconductor, in the TF approximation, the electrostatic potential energy of the donor electrons can be written as

$$V_{\text{TF}}(z) = -\frac{\alpha^2}{(\alpha|z| + z_0)^4} \quad (3)$$

with

$$\alpha = \frac{(2\bar{m})^{3/2} e^2 \nu}{60\pi^2 \epsilon_r \epsilon_0 \hbar^3} \quad (4)$$

and

$$z_0 = \left(\frac{8\alpha^3 \epsilon_r \epsilon_0}{e^2 n_D}\right)^{1/5}, \quad (5)$$

where z is distance perpendicular to the δ layer, ν is the number of equivalent conduction valleys, ϵ_r is the static dielectric constant, $\bar{m}$ is the geometric average of the longitudinal (m_l) and transverse (m_t) effective masses [31–34] ($\bar{m} = m_t^{2/3} m_l^{1/3}$), and n_D is the areal doping density.

To this TF potential is added an exchange potential (V_X) derived from the Dirac exchange energy functional [35] and a correlation potential (V_C). The exchange

potential is written as

$$V_X(z) = -\frac{\bar{m}e^4}{(4\pi\epsilon_r\epsilon_0\hbar)^2}\left(\frac{9}{4\pi^2}\right)^{1/3}\frac{1}{r_s(z)} \tag{6}$$

with

$$r_s(z) = \left[\frac{4\pi\bar{a_0}^3 n(z)}{3}\right]^{-1/3} \tag{7}$$

and

$$\bar{a_0} = \frac{4\pi\epsilon_r\epsilon_0\hbar^2}{\bar{m}e^2}, \tag{8}$$

where r_s is the Wigner-Seitz radius, $\bar{a_0}$ is the effective Bohr radius [$\bar{a_0} = 1.96$ nm for Si and $\bar{a_0} = 3.80$ nm for Ge, calculated using Eq. (8) and the parameters of Table I], and $n(z)$ is electron density (defined in Appendix). The correlation energy is approximated using the correlation functional parametrized by Perdew and Wang [36] for systems having zero spin polarization. In the high-density limit, this correlation potential is written as

$$V_C(z) = -2A\left\{\ln\left(1+\frac{1}{2Af}\right)\left(1+\frac{2\alpha_1 r_s(z)}{3}\right) - \frac{f'}{f(1+2Af)}\left[\frac{r_s(z)(1+\alpha_1 r_s(z))}{3}\right]\right\} \tag{9}$$

with

$$f = \beta_1 r_s^{1/2} + \beta_2 r_s + \beta_3 r_s^{3/2} + \beta_4 r_s^2 \tag{10}$$

and

$$f' = \frac{\beta_1}{2} r_s^{-1/2} + \beta_2 + \frac{3\beta_3}{2} r_s^{1/2} + 2\beta_4 r_s, \tag{11}$$

where $A = 0.031091$, $\alpha_1 = 0.21370$, $\beta_1 = 7.5957$, $\beta_2 = 3.5876$, $\beta_3 = 1.6382$, and $\beta_4 = 0.49294$.

Finally, the donor potential is written,

$$V(z) = V_{TF}(z) + V_X(z) + V_C(z) \tag{12}$$

and in matrix form as

$$\hat{V} = \sum_i V_i\, c_i^\dagger c_i, \tag{13}$$

where V_i is the discrete form of $V(z)$ for the z coordinate. The Hamiltonian describing the doped system is therefore written as

$$\hat{H} = \hat{H}_{\text{bulk}} + \hat{V}. \tag{14}$$

Where the donor potential is treated as an external potential and added to the diagonal terms of the Hamiltonian matrix only [28,29], an approximation we believe to be validated by the results of the TF method as shown in Sec. III.

C. Fermi level of the doped system

Recent measurements of the band structure of a Si:P δ layer show at least one occupied state in the CB [13]. Because high density δ-doped Si:P layers exhibit metallic characteristics at low temperatures ($T \approx 4$ K), the Fermi level must be solved for iteratively. The number of occupied CB states is increased from zero until the charge neutrality condition is satisfied, i.e., inside a finite area, the number of donor electrons is equal to the number of donor atoms (each donor atom donating one donor electron). The energy at which charge neutrality is achieved is defined as the Fermi level.

The total number of donor electrons can be written,

$$N_T(E_F) = s\int_{E_{\min}}^{E_F} Z(E)\, f(E)\, dE, \tag{15}$$

where E_F is the Fermi level, s is the spin degeneracy, $E_{\min}$ is the energy of the lowest occupied CB state, $Z(E)$ is the eDOS evaluated over the first 2D BZ, and $f(E)$ is the Fermi function. Substituting in for $f(E)$ and setting s equal to one, leads to

$$N_T(E_F) = \int_{E_{\min}}^{E_F} Z(E)\left[1+\exp\left(\frac{E-E_F}{k_B T}\right)\right]^{-1} dE, \tag{16}$$

where k_B is Boltzmann's constant and T is temperature. The area of the first 2D BZ is converted to a real space area and the number of donors is calculated from the areal doping density. E_F is then solved for iteratively by evaluating Eq. (16) at values for E_F greater than $E_{\min}$ until charge neutrality is achieved.

III. THOMAS-FERMI MODEL OF A δ-DOPED Si:P MONOLAYER IN THE HIGH-DENSITY LIMIT

One of the earliest applications of the TF theory [37–39] to δ-doped semiconductors was its application to an n-type δ layer [30]. Later, the same TF method was applied to p-type δ layers in GaAs and Si [40] and Si and B δ layers in GaAs [29]. The transport properties of n-type δ layers in Si have also been studied using this TF method [32]. Si:P δ layers were first modeled using a DFT method with a planar Wannier orbital (PWO) basis [41], and later, an antibonding orbital basis [42] with an sp^3s^* TB model [43]. However, the sp^3s^* basis set is too small to reproduce the experimentally predicted curvature of the X conduction valley minima [19]. A self-consistent three-dimensional (3D) quantum well method [44] combined with an $sp^3d^5s^*$ TB model[16] was therefore recently used in both studies of disorder and temperature dependence in Si:P δ layers [45,46]. These investigations used the NEMO 3-D package [47], which has more recently been applied to δ-doped Si:P quantum wires [9,48]. Complementary DFT models of Si:P δ layers and quantum wires have also been proposed using the SIESTA and VASP packages, with a basis of localized atomic orbitals (LAO) [23,24,49–51] and a plane-wave basis [23]. However, the applicability of these models to realistic device architectures is restricted by a N^3 scaling in calculation time (characteristic of DFT). Historically, the EMT has also been used to study n-type δ-doped layers [33] and was recently put on a firm theoretical footing for Si:P δ layers [31].

Figure 1 shows the band structure of bulk Si plotted in the face-centred cubic (fcc) BZ on a path of high symmetry [52] from L to Γ to X_{fcc}. Si is an indirect band-gap semiconductor and has a sixfold degenerate CB minimum at $0.81X_{\text{fcc}}$. Figure 2 shows the band structure (CB only) of a Si:P δ layer plotted in the PT BZ from $0.3M$ to Γ to $0.6X_{\text{pt}}$. Transforming from an fcc unit cell to a PT supercell projects the $\pm k_z$ conduction valleys to Γ. These bands are labeled as 1Γ and 2Γ in Fig. 2. Doping the bulk system increases the electron confinement (perpendicular to the dopant plane) and perturbs the $\pm k_z$ valleys; lifting their degeneracy and shifting them into the

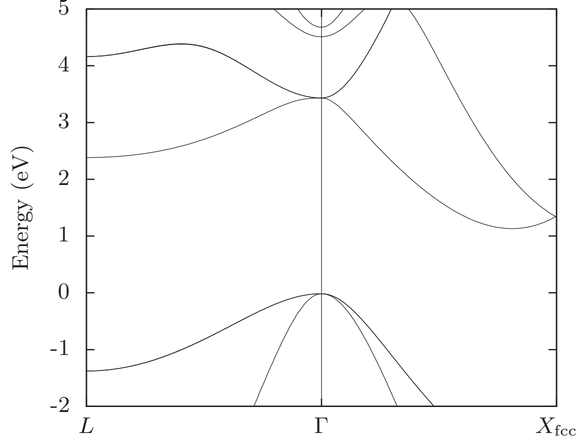

FIG. 1. The band structure of bulk Si calculated using an $sp^3d^5s^*$ TB method [16]. The energy bands are plotted on a high-symmetry path in the fcc BZ.

bulk band-gap region. In Fig. 2, the minima of the $\pm k_z$ valleys are split by the $1\Gamma/2\Gamma$ valley splitting [24] (which is here equal to $E_{2\Gamma} - E_{1\Gamma}$). The $\pm k_x$ and $\pm k_y$ valleys are also affected by unit cell representation. The $0.81X_{\text{fcc}}$ valley minimum appears at $0.37X_{\text{pt}}$ in Fig. 2. This valley is labeled as 1Δ and is also shifted into the bulk band-gap region by the 1D confinement.

The 1D confinement of electrons by the donor potential shifts the lowest bulk Si CB states into the bulk band-gap region. Figure 2 shows three main conduction valleys to be partially occupied, or partly below the Fermi level (E_F); these are the 1Γ, 2Γ, and 1Δ bands. The energy minima of these bands and those predicted by other models are shown in Table II. The energy minimum of the 1Γ band or CB minimum ($E_{1\Gamma}$) is 285 meV below the Fermi level (E_F), which suggests that the Si:P δ layer is metallic. $E_{1\Gamma}$ is 427 meV below the CB minimum of bulk Si and agrees with the results of all models [excluding DFT1D (LAO) and DFT3D (LAO)] to within 28 meV. The minimum of the 2Γ band ($E_{2\Gamma}$)

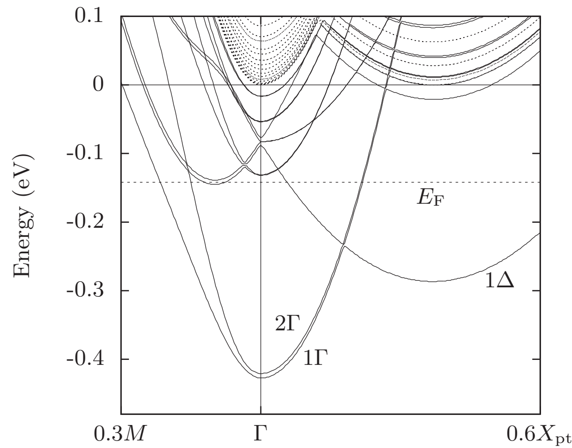

FIG. 2. The band structure of the Si:P δ layer (with $n_D = 1/4$ ML) (solid lines) and the Fermi level (at $T = 4$ K) (dashed line). The energy bands are plotted in the PT BZ and only the 12 lowest conduction bands are shown. The energy axis has been offset so that the energy of the bulk Si CB minimum is at energy zero. The band structure of bulk Si is also shown (dotted lines).

TABLE II. Band energy minima and Fermi levels (meV) for a range of Si:P δ layer models (with $n_D = 1/4$ ML and $T \approx 4$ K). This work is highlighted in bold. The TB3D model is published in Ref. [45], however, the results in this table are from the more recently published Ref. [48].

Model (basis set)	$E_{1\Gamma}$	$E_{2\Gamma}$	$E_{1\Delta}$	E_F
DFT1D (LAO) [a]	−296	−288	−165	−72
DFT3D (LAO) [b]	−369	−269	−68	−23
TB3D ($sp^3d^5s^*$) [c]	−401	−375	−249	−115
DFT1D (PWO) [d]	−419	−394	−250	−99
TF ($sp^3d^5s^*$)	**−427**	**−421**	**−287**	**−142**
EMT1D [e]	−445	−426	−257	N/A

[a]Reference [49] (read directly from plots with an uncertainty of ±3 meV).
[b]Reference [23].
[c]Reference [45].
[d]Reference [41] (read directly from plots with an uncertainty of ±3 meV).
[e]Reference [31] (read directly from plots with an uncertainty of ±3 meV).

compares equally well to DFT1D (PWO) and is within 5 meV of EMT1D. Interestingly, the 1Δ band minimum ($E_{1\Delta}$) of the TF method is 30–38 meV lower than those predicted by the three closest models in Table II. In general, for the band energy minima, there is good agreement between the models and the TF method. However, values for E_F differ significantly between the models. This disparity can be explained by the variation in the method and $\vec{k}$-point grid used to solve for E_F in each model. To calculate E_F, we use a similar method to TB3D and although the TF method predicts a E_F which is 27 meV lower than that of TB3D, this difference can be explained by the 26 meV discrepancy in the values for $E_{1\Gamma}$. The calculated binding energies ($E_F - E_{1\Gamma}$) of TB3D and the TF method agree within 1 meV (see Table III).

TABLE III. Valley splittings and binding energies (meV) for a range of Si:P δ layer models (with $n_D = 1/4$ ML and T ≈ 4K) and experiment (with $T \approx 100$ K). This work is highlighted in bold. The TB3D model is published in Ref. [45], however, the results in this table are from the more recently published Ref. [48].

Model (basis set)	$E_{2\Gamma} - E_{1\Gamma}$	$E_F - E_{1\Gamma}$
DFT1D (LAO)[a]	8	224
Experiment [b]	N/A	∼270
TF ($sp^3d^5s^*$)	**6**	**285**
TB3D ($sp^3d^5s^*$) [c]	26	286
DFT1D (PWO) [d]	25	320
DFT3D (LAO) [e]	100	346
EMT1D [f]	19	470[†]

[a]Reference [49] (read directly from plots with an uncertainty of ±6 meV).
[b]Reference [13].
[c]Reference [45].
[d]Reference [41] (read directly from plots with an uncertainty of ±6 meV).
[e]Reference [23].
[f]Reference [31].

A number of factors may contribute to the differences in the band energy minima shown in Table II. These include the basis set size [23], central-cell corrections [31,53], and the methods used to approximate the exchange and correlation (XC) energies. In the DFT models, the size of the localized atomic orbital basis set has been shown to be an important factor in the calculation of the band energy minima. For example, it was shown that the explicit atom model of Ref. [49] overestimates the $1\Gamma/2\Gamma$ valley splitting by approximately 50% when compared to a model that used a more complete basis [23]. Similarly, it is likely that central-cell corrections (and the resultant valley-orbit interaction) also contribute to the differences between the models. In TB3D and the TF method (and EMT1D), the donor atoms are described as point charges and an infinitely thin sheet of charge, respectively. This is a bad approximation close to the donor atoms or dopant plane, where the donor potential is quickly varying. However, in the DFT models, pseudopotentials are used, which model the valence *and* core electrons and therefore incorporate "central-cell" effects; although central-cell corrections will be weak for Si:P, which is a shallow donor [31].

Another contributing factor is the arrangement of donor atoms and whether they are modeled implicitly or explicitly. All explicit models in Table II use a perfectly ordered arrangement of donor atoms and therefore, as in the case of the implicit models, short- and long-range symmetries are preserved. However, in the implicit models, the variation of the donor potential inside the dopant plane disappears, as do any effects of this variation. Finally, excluding EMT1D and the TF method, each of the models in Table II use different methods to approximate the XC energy. The band energy minimum, $E_{1\Gamma}$, calculated in DFT1D (PWO), shifts by 10 ± 3 meV due to XC (and short-range) effects. This is compared to a -34 meV shift in the $E_{1\Gamma}$ of TB3D (see Refs. [45,46]) when XC energy corrections are made to the donor potential. However, these energy shifts are relatively small compared to the -130 meV shift in $E_{1\Gamma}$ that corresponds to adding XC corrections to the TF potential.

Figure 3 shows the TF potential with and without XC corrections, and the Fermi level and band energy minima inside the donor potential with XC corrections. XC effects increase the magnitude of the TF potential. The effect of exchange is far greater than that of correlation at a doping density of 1/4 ML. The exchange potential shifts the energy of $E_{1\Gamma}$ by -125 meV, where as the correlation potential shifts the energies by only -5 meV. Therefore, at a doping density of 1/4 ML, a TF potential with a Dirac exchange correction is adequate to describe the Si:P δ layer.

The 1D confinement of the electrons by the donor potential also lifts the degeneracy of the $\pm k_z$ valley minima and results in a valley splitting between the 1Γ and 2Γ bands, named the $1\Gamma/2\Gamma$ valley splitting [49]. Understanding this energy splitting is important in the design of "few-electron" quantum electronics in silicon [54] and modeling transport properties in these nanostructures at low-voltage biases [55]. Table III shows the $1\Gamma/2\Gamma$ valley splitting ($E_2 - E_1$) calculated by a range of Si:P δ layer models. The valley splitting predicted by the TF method is 6 meV and agrees with that of DFT1D (LAO) to within 2 ± 6 meV. There is a difference of 20 meV between the valley splitting calculated by TB3D and the TF method.

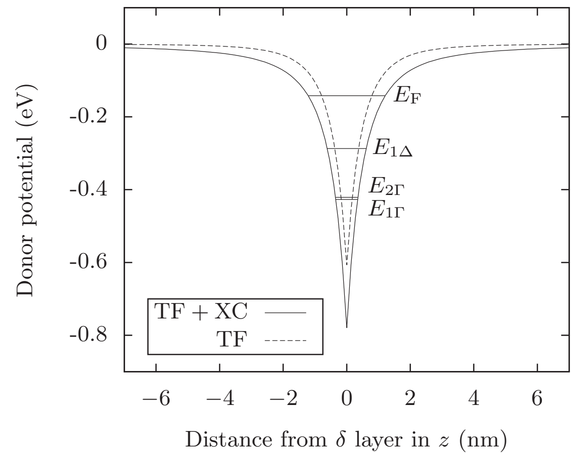

FIG. 3. TF potential for a Si:P δ layer (with $n_D = 1/4$ ML) with (solid line) and without (dashed line) XC corrections. The Fermi level and band energy minima are shown inside the potential well for the donor potential with XC corrections.

There are also differences of 14 ± 6 and 21 ± 6 meV between the valley splittings calculated by EMT1D and DFT1D (PWO), respectively, and the TF method. Again, these discrepancies can be explained by a number of factors; such as basis set size, central-cell corrections, and especially, valley-orbit coupling. Interestingly, in Si:P δ layer systems with multiple layers, the valley splitting has been shown to be inversely proportional to the spatial extent of donors perpendicular to the doping plane [50]. Another factor that affects the size of the $1\Gamma/2\Gamma$ valley splitting is the doping density, in proportion to which the energy splitting can vary nonlinearly [31]. Understanding this relationship is therefore important for engineering valley splitting in Si:P δ layers.

Figure 4 shows the changes in Fermi level, band energy minima, valley splitting and binding energy ($E_F - E_1$) as the

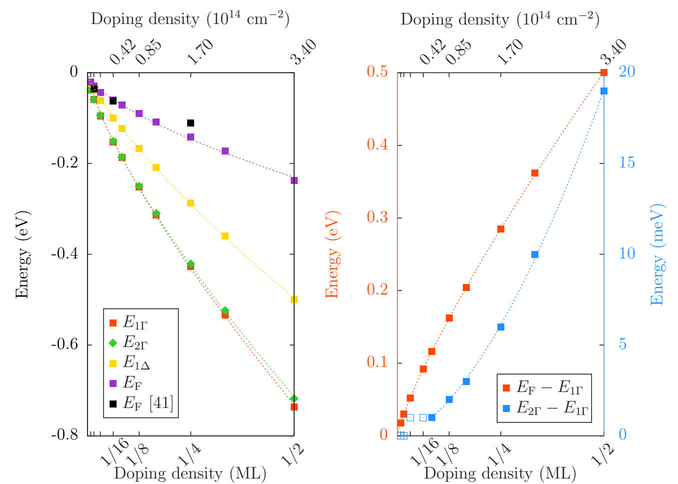

FIG. 4. (Color online) (Left) Band energy minima and the Fermi level plotted against doping density for a Si:P δ layer. The bulk Si CB minimum is at energy zero. (Right) Binding energy (red axis) and valley splitting (blue axis) plotted against doping density for a Si:P δ layer. The filled squares represent data points used to calculate the nonlinear fits (dotted lines).

doping density is varied. The range of doping densities has been limited at low doping densities by the applicability of the TF theory, and at high doping densities by experiment. In Fig. 4, left, the variation in each of the energy-band minima was fitted with an equation of the form

$$E_n = a(n_D)^b, \tag{17}$$

where E_n is the minimum energy of band n, and a and b are fitting parameters. A goodness of fit (R^2) of greater than 0.999 was obtained for the fit of each band energy. For the 1Γ, 2Γ and 1Δ bands, the relationship between E_n and n_D is nonlinear with b restricted to the closed interval [0.73, 0.78]. This agrees closely to the scaling theory of Ref. [31], which predicts $E_n \propto (n_D)^{2/3}$. In contrast, TB3D predicts a linear proportionality between E_n and n_D; however, this dependence is based on a relatively small total variation in the doping density—as in this explicit model the doping density is not a parameter which can be easily varied—and is therefore expected to be less accurate. We fitted the Fermi level using Eq. (17) and found that it also varies nonlinearly with doping density ($b = 0.66$, $R^2 = 0.995$). This is in contrast to Ref. [31] where no such trend is evident. From a comparison of the two E_F data sets in Fig. 4, left, it is obvious that the variation in the Fermi level agrees more closely with the results of Ref. [41] [DFT1D (PWO)].

A consequence of the nonlinear dependence of E_n on n_D for the band energy minima and Fermi level is that properties which are calculated directly from these values (such as the binding energy and valley splitting) exhibit a similar nonlinearity to changes in doping density. In Fig. 4, right, the change in the binding energy and valley splitting has been fitted using Eq. (17), and b has been found to be 0.82 and 1.64, respectively ($R^2 \geqslant 0.999$). However, the valley splitting data has only been fitted for $n_D \geqslant 1/12$ ML, as from an analysis of Fig. 4, right, it is obvious that the nonlinear variation in valley splitting breaks down at doping densities less than 1/12 ML—which is possibly due to the weaker electron confinement at these densities.

Recently published experimental measurements of the Si:P δ layer band structure performed at $T = 100$ K confirm the existence of at least one occupied state at Γ [13]. This state, named the δ state, has a binding energy of approximately 190 meV at $T = 300$ K and approximately 270 meV at $T = 100$ K. Comparison with the theory is difficult because all Si:P δ layer models explicitly assume lower temperatures ($T \approx 4$ K) and are buried under approximately 16 nm of Si cladding as opposed to the 2 nm of Si cladding used in experiment. However, it is obvious from Table III that the experimental binding energy of approximately 270 meV at $T = 100$ K is in good agreement with the value of 285 meV calculated using the TF method at $T = 4$ K. It is not obvious from the experimental measurements whether there is a valley splitting at Γ. However, the energy resolution of the experimental band structure measurement is low and energy splittings of less than approximately 100 meV are not resolvable.

IV. ELECTRONIC PROPERTIES OF A Ge:P δ LAYER IN THE HIGH-DENSITY LIMIT

The similar electronic properties of Ge and Si make Ge equally attractive for the manufacture of nanoelectronic devices. Carrying on from the successes of the δ-doped Si:P fabrication route, δ-doped Ge:P nanostructures are now being experimentally fabricated on the nanometre scale using similar *in situ* techniques [56,57]. Presently, experiments are focused on highly doped Ge:P monolayers [11,57,58] that could be used as the channel material in the next generation of high-speed nanotransistors [59]. Ultrascaled n-type Ge devices on the Si platform could also be realized through the patterning of Ge:P δ layers into source and drain contacts or quantum wires, as has been done for Si:P δ layers [8,9,60].

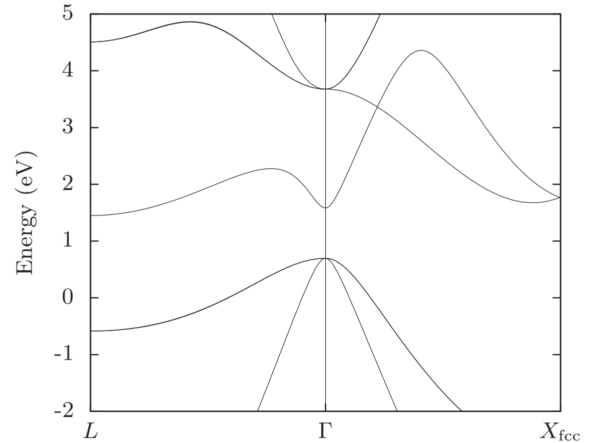

FIG. 5. Band structure of bulk Ge calculated using an $sp^3d^5s^*$ TB method [16]. The bands are plotted in the fcc BZ.

The bulk Ge band structure is shown in Fig. 5. Ge is an indirect band-gap semiconductor and has a fourfold degenerate CB minimum at L in the fcc BZ. Transforming from an fcc unit cell to a PT supercell folds the conduction valleys at L to M in the PT BZ. These bands are labeled as $1M$ and $2M$ in Fig. 6; where it is shown that in the Ge:P δ layer band structure, the lowest CB states of bulk Ge are shifted into the bulk band-gap region (as a result of the electron confinement by the donor potential). This electron confinement also results in a valley splitting of 16 meV between the $1M$ and $2M$ energy-band minima. As the Ge CB minimum is fourfold degenerate, the $1M$ and $2M$ bands are each doubly degenerate. Transforming from an fcc unit cell to a PT supercell also folds the bands in the $\pm k_x$ and $\pm k_y$ directions. The $0.88X_{\text{fcc}}$ valley minimum of bulk Ge is projected to $0.24X_{\text{pt}}$ in Fig. 6 (where this band is labeled as 1Δ). The $\pm k_z$ conduction valleys are folded to Γ and are labeled as 1Γ and 2Γ. The degeneracy of these bands is lifted and there is a valley splitting of 6 meV between them—which is equal to the 1Γ/2Γ valley splitting of the Si:P δ layer. Interestingly, the conduction valley at Γ in the bulk Ge band structure is not shifted into the bulk band-gap region to the same degree as the conduction valleys at M and X. This band is labeled as 3Γ in Fig. 6. Instead, the 1Γ and 2Γ bands form the local minima at Γ in the Ge:P δ layer band structure. Therefore, at low-voltage biases, we expect the transport properties of the Ge:P δ layer to be most strongly affected by the $1M$ and $2M$ bands at M and 1Γ and 2Γ bands at Γ.

The donor potential for the Ge:P δ layer is shown in Fig. 7. At a doping density of 1/4 ML the donor potential of the Ge:P δ layer is broader in z than that of the Si:P δ layer (which

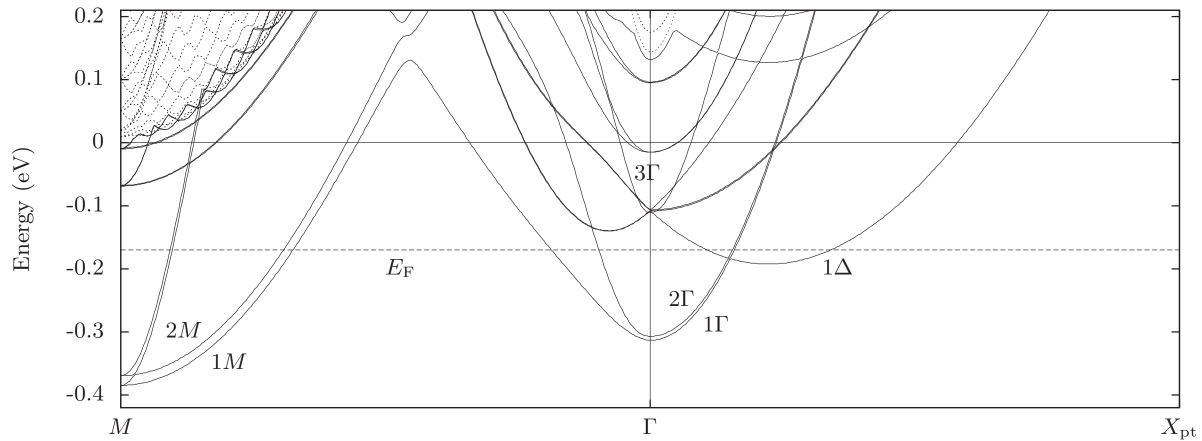

FIG. 6. The band structure of the Ge:P δ layer (with $n_D = 1/4$ ML) (solid lines) and the Fermi level (at $T = 4$ K) (dashed line). The energy bands are plotted in the PT BZ and only the 12 lowest conduction bands are shown. The energy axis has been offset so that the energy of the bulk Ge CB minimum is at energy zero. The band structure of bulk Ge is also shown (dotted lines).

is possibly due to the larger effective Bohr radius of Ge). However, the magnitudes of the donor potentials inside the dopant plane are similar; they are 0.85 and 0.78 eV for Ge and Si, respectively. Because the magnitude of the donor potential in Ge is greater than that in Si, we expect the CB minimum (E_{1M}) of the Ge:P δ layer to be shifted further into the bulk band-gap region than the CB minimum of the Si:P δ layer. However, from a comparison of the two band structures—the opposite is true—the 1Γ band in Fig. 2 is shifted further into the bulk band-gap region than the $1M$ band in Fig. 6. This can be explained by the broadening of the Ge:P δ layer potential, which decreases the confinement perpendicular to the dopant plane.

Figure 8 shows the eDOS of the Ge:P and Si:P δ layers. Ignoring energies around -0.25 eV, the eDOS of the Ge:P δ layer is greater than that of the Si:P δ layer on the closed interval $[-0.4, 0.0]$ eV. This can be explained by the greater number of partially occupied bands, or conducting modes, in the Ge:P δ layer band structure and suggests a higher conductivity for the Ge:P δ layer than the Si:P δ layer at low-voltage biases. The larger eDOS for the Si:P δ layer around $E = -0.25$ eV is due to the filling of the Si:P 1Δ band ($E_{1\Delta,\text{Si:P}} = -287$ meV) before the Ge:P 1Δ band ($E_{1\Delta,\text{Ge:P}} = -192$ meV).

In Figure 9, the change in the Fermi level, band energy minima, binding energy and valley splitting with doping density is shown for the Ge:P δ layer. The $1M$ and $2M$ energy minima, Fermi level, valley splitting and binding energy have been fitted using Eq. (17). However, because the energy minima of the 1Γ, 2Γ, 3Γ, and 1Δ bands are greater than the CB minimum of bulk Ge (which is offset at energy zero in Fig. 9, left,) these minima have been fitted using an equation of the form

$$E_n = a(n_D)^b + c, \tag{18}$$

where E_n is the minimum energy of band n, and a, b, and c are fitting parameters. The energy minima of the $1M$, $2M$, 1Γ, 2Γ, 3Γ, and 1Δ bands have been fitted with an

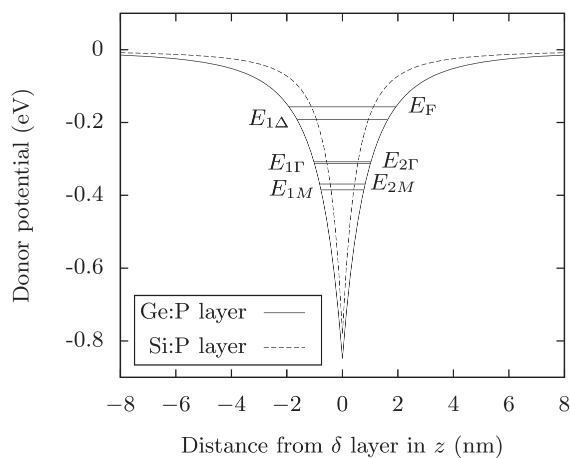

FIG. 7. Donor potential for a Ge:P δ layer (solid line) and Si:P δ layer ($n_D = 1/4$ ML) (dashed line). The Fermi level and band energy minima are shown inside the potential well for the Ge:P δ layer.

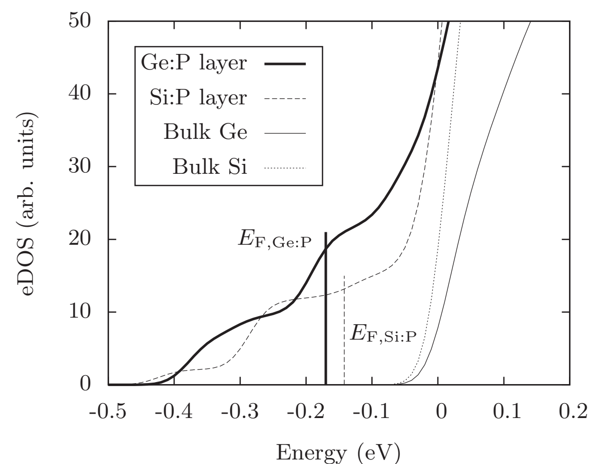

FIG. 8. eDOS of the Ge:P δ layer (heavy solid line) and Si:P δ layer (dashed line) (with $n_D = 1/4$ ML), and eDOS of bulk Ge (light solid line) and bulk Si (dotted line). A Gaussian smearing of 25 meV has been applied for visualization.

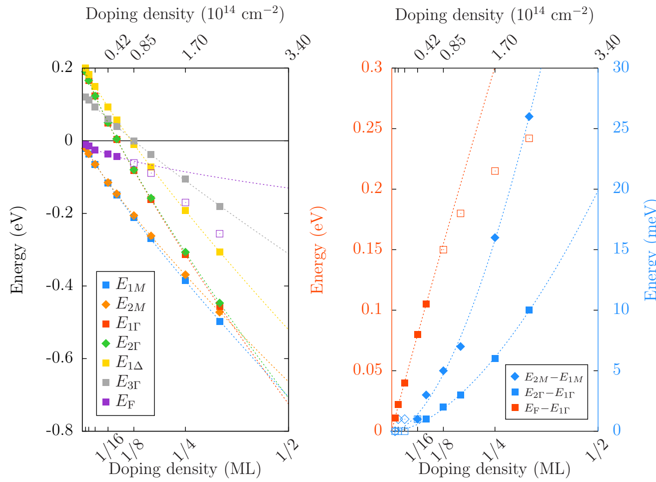

FIG. 9. (Color online) (Left) Band energy minima and the Fermi level plotted against doping density for a Ge:P δ layer. The bulk Ge CB minimum is at energy zero. (Right) Binding energy (red axis) and valley splitting (blue axis) plotted against doping density for a Ge:P δ layer. The filled squares represent data points used to calculate the nonlinear fits (dotted lines).

$R^2 \geqslant 0.9996$ and the fitting parameter b has been found to be restricted to the closed interval [0.81,0.91]. Therefore the nonlinear proportionality between the band energy minima and the doping density for the Ge:P δ layer is different to that of the Si:P δ layer. The Ge:P δ layer exhibits a greater rate of change in its band energy minima with doping density. Using the nonlinear fits of the energy-band data, we can estimate the value of the CB minimum at a doping density of 1/2 ML (which would otherwise be difficult to do due to the mixing of the CB and VB energy eigenvalues at this density). We find that the CB minimum of the Ge:P band structure is approximately −700 meV (relative to the CB minimum of bulk Ge) at a doping density of 1/2 ML. The fits to the band energy minima also suggest that the levels of the $1M/2M$ and $1\Gamma/2\Gamma$ bands converge at a density greater than 1/3 ML (although this is difficult to validate without explicitly calculating the band energy minima at higher density). However, the rate of change of the 1Γ and 2Γ energy minimum with doping density is greater than that for the other bands, which is possibly due to a greater sensitivity in the $\pm k_z$ valleys to the stronger electron confinement in z at higher doping densities. At $n_D \geqslant 1/16$ ML, the energy minima of the $1\Gamma/2\Gamma$ bands becomes lower than that of the 3Γ band and the $1\Gamma/2\Gamma$ bands become the new local minimum at Γ. The rate of change of the 3Γ energy minimum with doping density is smaller than that for the other bands.

The Fermi level has been fitted using Eq. (17) but with a reduced set of data points (filled squares). It is obvious from Fig. 9, left, that the simple nonlinear trend proposed using Eq. (17) breaks down at $n_D > 1/8$ ML. This discrepancy is due to the filling of the 1Γ, 2Γ, and 1Δ bands at these higher doping densities. Therefore, unlike the case of the Si:P δ layer, Eq. (17) is unable to describe the dependence of the Fermi level on doping density. Similarly, in Fig. 9, right, Eq. (17) is also unable to describe the dependence of the binding energy on doping density as the binding energy is calculated directly from the CB minimum *and* the Fermi level. At a doping density of 1/4 ML, the binding energy of the Ge:P δ layer is found to be 70 meV smaller than that of the Si:P δ layer. The $1M/2M$ valley splitting has been fitted for $n_D \geqslant 1/16$ ML using Eq. (17) and b has been found to be 1.74 ($R^2 = 0.9996$). The $1\Gamma/2\Gamma$ valley splitting has been fitted for $n_D \geqslant 1/12$ ML and b has been found to be 1.70 ($R^2 = 0.9991$). Both energy splittings show a similar nonlinear trend to the $1\Gamma/2\Gamma$ valley splitting of the Si:P δ layer.

V. CONCLUSIONS

We have presented a scalable method for the calculation of electronic properties in Si:P and Ge:P δ layers. In the derivation of the TF potential, self-consistency is achieved by insisting that the potential is related to the charge density by Poisson's equation. The computational expense of the calculations is thereby reduced—compared to other TB models—by removing the need to iteratively solve for the electrostatic field. The TFD theory is exact in the high density limit and we have found that this TF method is able to reproduce the results of more "resource intensive" computational models of Si:P δ layers. Therefore the TF method is both scalable to large system sizes and adequate to describe the physics of highly doped Si:P nanostructures. This is ideal for the calculation of quantum transport properties in these δ-doped semiconductors.

The Ge:P δ layer was shown to have conduction valley minima at M, Γ, and $0.24X$ in the PT BZ. A Ge:P δ state, analogous to the Si:P δ state [13], is predicted at M with a $1M/2M$ valley splitting of 16 meV. As this energy splitting is larger than the $1\Gamma/2\Gamma$ valley splitting of the Si:P δ layer, we expect experimental measurements to be more sensitive to the valley splitting of the lowest CB states in the Ge:P δ layer. The binding energy of this Ge:P δ state is found to be 70 meV smaller than the binding energy of the Si:P δ state and we therefore expect that this difference is experimentally resolvable. The Ge:P δ layer exhibits a larger number of occupied conducting modes compared to the Si:P δ layer. This suggests a higher conductivity for the Ge:P δ layer at low-voltage biases.

In the future, the TF method could be extended to δ-doped Si:P and Ge:P quantum wires, source and drain contacts, and other finite δ-doped nanostructures. Central-cell corrections (and the resultant valley-orbit interaction) could be included in the model to more accurately describe the electron confinement perpendicular to the dopant plane and the corresponding $1\Gamma/2\Gamma$ valley splitting. Electron spin could also be included *via* the TB model and the validity of the XC corrections could be investigated. However, these extensions would require higher precision in the experimental results than that which is currently available to successfully evaluate the validity of including these effects.

ACKNOWLEDGMENTS

The authors thank A. Budi and D.W. Drumm for useful discussions. The authors acknowledge the support of the NCI National Facility, Canberra, Australia.

APPENDIX: DERIVATION OF THE ELECTROSTATIC POTENTIAL ENERGY OF THE DONOR ELECTRONS IN THE THOMAS-FERMI APPROXIMATION

This appendix gives a derivation of the electrostatic potential energy of the donor electrons in the Thomas-Fermi approximation. In the following, n is the electron density, z is a coordinate that is perpendicular to the dopant plane and all quantities are expressed in SI units. For a more detailed explanation of the Thomas-Fermi theory and the Thomas-Fermi theory of semiconductors see Refs. [39] and [30].

The TF energy density functional is written as

$$E_{\mathrm{TF}}[n(z)] = T[n(z)] + U_{ee}[n(z)] + U_{e\mathrm{N}}[n(z)],$$

where $T[n(z)]$ is the kinetic energy density functional and $U_{ee}[n(z)]$ and $U_{e\mathrm{N}}[n(z)]$ are the electron-electron and electron-nuclear potential energy density functionals, respectively,

$$T[n(z)] = \int t\, dz, \tag{A1}$$

where t is the kinetic energy per unit volume,

$$t = \int_0^{p_{\mathrm{F}}} n(z)\, \frac{[p(z)]^2}{2\bar{m}}\, \frac{3[p(z)]^2}{[p_{\mathrm{F}}(z)]^3}\, dp\ . \tag{A2}$$

In the local density approximation,

$$n(z) = n_0 = \frac{N}{V}, \tag{A3}$$

where N is the number of electrons inside a real-space volume V. As a consequence of the uncertainty principle,

$$N = \frac{2}{h^3}\mathscr{V}\ . \tag{A4}$$

Here, $\mathscr{V}$ is the total volume of occupied phase space,

$$\mathscr{V} = \frac{4\pi\nu}{3}[p_{\mathrm{F}}(z)]^3 V,$$

where $p_{\mathrm{F}}(z)$ is the maximum momentum of an electron at z and ν is the degeneracy of the conduction valley minima.

Substituting this into Eq. (A4), we have

$$N = \frac{2}{h^3}\frac{4\pi\nu}{3}[p_{\mathrm{F}}(z)]^3 V$$

and, recalling Eq. (A3), we also have

$$n(z) = \frac{8\pi\nu}{3h^3}[p_{\mathrm{F}}(z)]^3\ . \tag{A5}$$

Rearranging Eq. (A5), we obtain

$$[p(z)]^5 = \left[\frac{3h^3}{8\pi\nu}n(z)\right]^{5/3}\ . \tag{A6}$$

Substituting Eqs. (A5) and (A6) into Eq. (A2) leads to

$$t = c_k[n(z)]^{5/3}, \tag{A7}$$

where

$$c_k = \frac{3}{10\bar{m}\nu^{2/3}}(3\pi^2\hbar^3)^{2/3}\ .$$

Substituting Eq. (A7) into Eq. (A1), the kinetic energy density functional can be written as

$$T[n(z)] = c_k \int n(z)^{5/3}\, dz\ .$$

The electron-electron potential energy density functional is defined as

$$U_{ee}[n(z)] = \frac{e^2}{8\pi\epsilon_r\epsilon_0}\iint \frac{n(\vec{r}')n(\vec{r})}{|\vec{r}-\vec{r}'|}\, d\vec{r}\, d\vec{r}'\ .$$

For an infinite plane of charge, this can be written as

$$U_{ee}[n(z)] = -\frac{e^2}{4\epsilon_r\epsilon_0}\iint n(z)\, n(z')\, |z-z'|\, dz\, dz'\ .$$

The electron-nuclear potential energy density functional is defined as

$$U_{eN}[n(z)] = e\int n(\vec{r})V_{\mathrm{N}}(\vec{r})\, d\vec{r}\ .$$

For an infinite plane of charge this can be written as

$$U_{eN}[n(z)] = -\frac{e^2 n_D}{2\epsilon_r\epsilon_0}\int n(z)\, |z|\, dz\ .$$

Substituting these into the TF energy-density functional, we get

$$E_{\mathrm{TF}}[n(z)] = c_k\int n(z)^{5/3}\, dz - \frac{e^2 n_D}{2\epsilon_r\epsilon_0}\int n(z)\,|z|\, dz - \frac{e^2}{4\epsilon_r\epsilon_0}\iint n(z)\, n(z')\, |z-z'|\, dz\, dz'\ . \tag{A8}$$

The variational principle can be used to find $n(z)$ for the ground-state energy by minimizing Eq. (A8) subject to the constraint that N is constant. This is written as

$$\delta(E-\mu N) = 0$$

or

$$\mu = \frac{\partial E}{\partial N},$$

where μ is the chemical potential energy. The total number of electrons can be written as

$$N = \int n(z)\, dz\ .$$

From this and Eq. (A8), it follows that

$$\mu = \frac{5}{3}c_k\{n(z)\}^{2/3} - \frac{e^2 n_D}{2\epsilon_r\epsilon_0}|z| - \frac{e^2}{2\epsilon_r\epsilon_0}\int n(z)|z-z'|\, dz\ . \tag{A9}$$

We define the electrostatic part of Eq. (A9) as

$$V_{\mathrm{TF}}(z) = -\frac{e^2 n_D}{2\epsilon_r\epsilon_0}|z| - \frac{e^2}{2\epsilon_r\epsilon_0}\int n(z)|z-z'|\, dz\ . \tag{A10}$$

Therefore

$$\mu = \tfrac{5}{3}c_k[n(z)]^{2/3} + V_{\mathrm{TF}}(z)\ . \tag{A11}$$

The self-consistency of the electrostatic field in z is then achieved by insisting $V_{\mathrm{TF}}(z)$ and $n(z)$ are related by Poisson's equation:

$$\frac{\partial^2}{\partial z^2}\Phi(z) = -\frac{\rho(z)}{\epsilon_r\epsilon_0}, \tag{A12}$$

$$\frac{\partial^2}{\partial z^2}[e\Phi(z)] = -\frac{e\rho(z)}{\epsilon_r\epsilon_0}, \tag{A13}$$

$$\frac{\partial^2}{\partial z^2}V_{\rm TF} = -\frac{e\rho(z)}{\epsilon_r\epsilon_0}. \tag{A14}$$

Taking the double derivative of Eq. (A10) in z,

$$\frac{\partial^2}{\partial z^2}V_{\rm TF}(z) = \frac{e^2}{\epsilon_r\epsilon_0}n(z) - \frac{e^2 n_D}{\epsilon_r\epsilon_0}\delta(z), \tag{A15}$$

where

$$\rho(z) = e[n_D\delta(z) - n(z)]. \tag{A16}$$

Rearranging Eq. (A11) for $n(z)$,

$$n(z) = \left(\frac{3}{5c_k}\right)^{3/2}[\mu - V_{\rm TF}(z)]^{3/2},$$

and substituting it into Eq. (A15),

$$\frac{\partial^2}{\partial z^2}V_{\rm TF}(z) = \frac{e^2}{\epsilon_r\epsilon_0}\left(\frac{3}{5c_k}\right)^{3/2}[\mu - V_{\rm TF}(z)]^{3/2} - \frac{e^2 n_D}{\epsilon_r\epsilon_0}\delta(z). \tag{A17}$$

The solution to Eq. (A17) is of the form

$$V_{\rm TF}(z) - \mu = -\frac{\alpha^2}{(\alpha|z| + z_0)^4},$$

where

$$\alpha = \frac{(2\bar{m})^{3/2}e^2\nu}{60\pi^2\epsilon_r\epsilon_0\hbar^3}$$

and

$$z_0 = \left(\frac{8\alpha^3\epsilon_r\epsilon_0}{e^2 n_D}\right)^{1/5}.$$

Setting μ equal to zero results in the following expression for the electrostatic potential energy of the donor electrons:

$$V_{\rm TF}(z) = -\frac{\alpha^2}{(\alpha|z| + z_0)^4}.$$

[1] H. F. Wilson, O. Warschkow, N. A. Marks, N. J. Curson, S. R. Schofield, T. C. G. Reusch, M. W. Radny, P. V. Smith, D. R. McKenzie, and M. Y. Simmons, Phys. Rev. B **74**, 195310 (2006).

[2] G. Scappucci, O. Warschkow, G. Capellini, W. M. Klesse, D. R. McKenzie, and M. Y. Simmons, Phys. Rev. Lett. **109**, 076101 (2012).

[3] J. R. Tucker and T.-C. Shen, Solid-State Electron. **42**, 1061 (1998).

[4] J. L. O'Brien, S. R. Schofield, M. Y. Simmons, R. G. Clark, A. S. Dzurak, N. J. Curson, B. E. Kane, N. S. McAlpine, M. E. Hawley, and G. W. Brown, Phys. Rev. B **64**, 161401 (2001).

[5] T.-C. Shen, J.-Y. Ji, M. A. Zudov, R.-R. Du, J. S. Kline, and J. R. Tucker, Appl. Phys. Lett. **80**, 1580 (2002).

[6] M. Füchsle, S. Mahapatra, F. A. Zwanenburg, M. Friesen, M. A. Eriksson, and M. Y. Simmons, Nat. Nanotechnol. **5**, 502 (2010).

[7] A. Fuhrer, M. Füchsle, T. C. Reusch, B. Weber, and M. Y. Simmons, Nano Lett. **9**, 707 (2009).

[8] S. R. McKibbin, G. Scappucci, W. Pok, and M. Y. Simmons, Nanotechnol. **24**, 045303 (2013).

[9] B. Weber, S. Mahapatra, H. Ryu, S. Lee, A. Fuhrer, T. C. Reusch, D. L. Thompson, W. C. T. Lee, G. Klimeck, L. C. L. Hollenberg, and M. Y. Simmons, Science **335**, 64 (2012).

[10] F. J. Rueß, B. Weber, K.-E. J. Goh, O. Klochan, A. R. Hamilton, and M. Y. Simmons, Phys. Rev. B **76**, 085403 (2007).

[11] G. Scappucci, G. Capellini, W. M. Klesse, and M. Y. Simmons, Nanotechnol. **22**, 375203 (2011).

[12] G. Scappucci, G. Capellini, W. M. Klesse, and M. Y. Simmons, J. Cryst. Growth **316**, 81 (2011).

[13] J. A. Miwa, P. Hofmann, M. Y. Simmons, and J. W. Wells, Phys. Rev. Lett. **110**, 136801 (2013).

[14] I. N. Remediakis and E. Kaxiras, Phys. Rev. B **59**, 5536 (1999).

[15] V. I. Anisimov, J. Zaanen, and O. K. Andersen, Phys. Rev. B **44**, 943 (1991).

[16] T. B. Boykin, G. Klimeck, and F. Oyafuso, Phys. Rev. B **69**, 115201 (2004).

[17] E. H. Hwang and S. Das Sarma, Phys. Rev. B **87**, 125411 (2013).

[18] S. Datta, *Quantum Transport: Atom to Transistor*, 1st ed. (Cambridge University Press, Cambridge, 2006).

[19] J.-M. Jancu, R. Scholz, F. Beltram, and F. Bassani, Phys. Rev. B **57**, 6493 (1998).

[20] J. C. Slater and G. F. Koster, Phys. Rev. **94**, 1498 (1954).

[21] G. Klimeck, R. Bowen, T. B. Boykin, C. Salazar-Lazaro, T. A. Cwik, and A. Stoica, Superlattices Microstruct. **27**, 77 (2000).

[22] R. Ramiarez and M. C. Bohm, Int. J. Quantum Chem. **30**, 391 (1986).

[23] D. W. Drumm, A. Budi, M. C. Per, S. P. Russo, and L. C. L. Hollenberg, Nanoscale research letters **8**, 111 (2013).

[24] D. J. Carter, O. Warschkow, N. A. Marks, and D. R. McKenzie, Phys. Rev. B **79**, 033204 (2009).

[25] R. Faulkner, Phys. Rev. **184**, 713 (1969).

[26] J. Hensel, H. Hasegawa, and M. Nakayama, Phys. Rev. **138**, A225 (1965).

[27] B. Levinger and D. Frankl, J. Phys. Chem. Solids **20**, 281 (1961).

[28] M. Graf and P. Vogl, Phys. Rev. B **51**, 4940 (1995).

[29] S. J. Vlaev and L. M. Gaggero-Sager, Phys. Rev. B **58**, 1142 (1998).

[30] L. Ioriatti, Phys. Rev. B **41**, 8340 (1990).

[31] D. W. Drumm, L. C. L. Hollenberg, M. Y. Simmons, and M. Friesen, Phys. Rev. B **85**, 155419 (2012).

[32] I. Rodríguez-Vargas and L. M. Gaggero-Sager, J. Appl. Phys. **99**, 033702 (2006).

[33] L. M. R. Scolfaro, D. Beliaev, R. Enderlein, and J. R. Leite, Phys. Rev. B **50**, 8699 (1994).

[34] W. Brinkman and T. Rice, Phys. Rev. B **7**, 1508 (1973).

[35] P. A. M. Dirac, Math. Proc. Cambridge **26**, 376 (1930).

[36] J. P. Perdew and Y. Wang, Phys. Rev. B **45**, 13244 (1992).

[37] L. H. Thomas, Math. Proc. Cambridge **23**, 542 (1927).

[38] E. Fermi, Zeitschrift für Physik **48**, 73 (1928).

[39] N. H. March, in *Theory of the Inhomogeneous Electron Gas*, edited by S. Lundqvist and N. H. March (Plenum Press, New York, 1983), Chap. 1, pp. 1–7.

[40] L. M. Gaggero-Sager, M. E. Mora-Ramos, and D. A. Contreras-Solorio, Phys. Rev. B **57**, 6286 (1998).
[41] G. Qian, Y.-C. Chang, and J. R. Tucker, Phys. Rev. B **71**, 045309 (2005).
[42] Y.-C. Chang and G. Li, Comput. Phys. Commun. **95**, 158 (1996).
[43] X. Cartoixà and Y.-C. Chang, Phys. Rev. B **72**, 125330 (2005).
[44] R. Rahman, C. J. Wellard, F. R. Bradbury, M. Prada, J. H. Cole, G. Klimeck, and L. C. L. Hollenberg, Phys. Rev. Lett. **99**, 036403 (2007).
[45] S. Lee, H. Ryu, H. Campbell, L. C. L. Hollenberg, M. Y. Simmons, and G. Klimeck, Phys. Rev. B **84**, 205309 (2011).
[46] H. Ryu, S. Lee, and G. Klimeck, in *13th International Workshop on Computational Electronics* (2009), pp. 1–4.
[47] G. Klimeck, S. S. Ahmed, H. Bae, N. Kharche, R. Rahman, S. Clark, B. Haley, S. Lee, M. Naumov, H. Ryu, F. Saied, M. Prada, M. Korkusinski, and T. B. Boykin, in *IEEE Transactions on Electron Devices* (2007), pp. 2079–2089.
[48] H. Ryu, S. Lee, B. Weber, S. Mahapatra, L. C. L. Hollenberg, M. Y. Simmons, and G. Klimeck, Nanoscale (2013), doi:10.1039/c3nr01796f.
[49] D. J. Carter, N. A. Marks, O. Warschkow, and D. R. McKenzie, Nanotechnol. **22**, 065701 (2011).
[50] A. Budi, D. W. Drumm, M. C. Per, A. Tregonning, S. P. Russo, and L. C. L. Hollenberg, Phys. Rev. B **86**, 165123 (2012).
[51] D. W. Drumm, J. S. Smith, M. C. Per, A. Budi, L. C. L. Hollenberg, and S. P. Russo, Phys. Rev. Lett. **110**, 126802 (2013).
[52] C. J. Bradley and A. P. Cracknell, *The Mathematical Theory of Symmetry in Solids: Representation Theory for Point Groups and Space Groups*, 1st ed. (Oxford University Press, London, 1972).
[53] M. Friesen, Phys. Rev. Lett. **94**, 186403 (2005).
[54] R. Rahman, J. Verduijn, N. Kharche, G. P. Lansbergen, G. Klimeck, L. C. L. Hollenberg, and S. Rogge, Phys. Rev. B **83**, 195323 (2011).
[55] M. Füchsle, J. A. Miwa, S. Mahapatra, H. Ryu, S. Lee, O. Warschkow, L. C. L. Hollenberg, G. Klimeck, and M. Y. Simmons, Nat. Nanotechnol. **7**, 242 (2012).
[56] G. Scappucci, G. Capellini, B. Johnston, W. M. Klesse, J. A. Miwa, and M. Y. Simmons, Nano Lett. **11**, 2272 (2011).
[57] G. Scappucci, G. Capellini, W. M. Klesse, and M. Y. Simmons, Nanoscale **5**, 2600 (2013).
[58] G. Scappucci, G. Capellini, W. C. T. Lee, and M. Y. Simmons, Appl. Phys. Lett. **94**, 162106 (2009).
[59] Y. Kamata, Materials Today **11**, 30 (2008).
[60] G. Scappucci, W. M. Klesse, A. R. Hamilton, G. Capellini, D. L. Jaeger, M. R. Bischof, R. F. Reidy, B. P. Gorman, and M. Y. Simmons, Nano Lett. **12**, 4953 (2012).